Ori Henderson-Sapir, Jesper Munch, and David J. Ottaway
New energy-transfer upconversion process in Er^{3+}:ZBLAN mid-infrared fiber lasers
Optics Express, 2016; 24(7):6869-6883

Published version: http://dx.doi.org/10.1364/OE.24.006869

A new energy-transfer upconversion process in Er^{3+}:ZBLAN mid-infrared fiber lasers

Ori Henderson-Sapir, Jesper Munch and David J. Ottaway

School of Physical Sciences and Institute for Photonics and Advanced Sensing (IPAS), The University of Adelaide, SA 5005, Australia

*ori.henderson-sapir@adelaide.edu.au

Abstract: We report a new energy-transfer process in erbium doped ZBLAN glass, which is critical for optimizing the operation of lasers that use the 3.5 μm band $^4F_{9/2}$ to $^4I_{9/2}$ transition. The magnitude of this energy-transfer process is measured for two different doping levels in Er^{3+}:ZBLAN and the requirement for low doping in these lasers established.

OCIS codes: (060.2390) Fiber optics, infrared; (060.2410) Fibers, erbium; (060.3510) Lasers, fiber; (140.3480) Lasers, diode-pumped.

References and links

1. V. Fortin, M. Bernier, S. T. Bah, and R. Valle, "30 *W* fluoride glass all-fiber laser at 2.94 μm," Opt. Lett. **40**, 2882–2885 (2015).
2. O. Henderson-Sapir, J. Munch, and D. J. Ottaway, "Mid-infrared fiber lasers at and beyond 3.5 μm using dual-wavelength pumping," Opt. Lett. **39**, 493–496 (2014).
3. V. Fortin, F. Maes, M. Bernier, S. T. Bah, M. D'Auteuil and R. Vallée, "Watt-level erbium-doped all-fiber laser at 3.44 μm," Opt. Lett. (to be published).
4. O. Henderson-Sapir, S. D. Jackson and D. J. Ottaway, "Versatile and widely tunable mid-infrared erbium doped ZBLAN fiber laser," (submitted to Opt. Lett).
5. P. S. Golding, S. D. Jackson, T. A. King, and M. Pollnau, "Energy transfer processes in Er^{3+}-doped and Er^{3+}, Pr^{3+}-codoped ZBLAN glasses," Phys. Rev. B **62**, 856–864 (2000).
6. M. Gorjan, M. Marincek, and M. Copic, "Role of interionic processes in the efficiency and operation of erbium-doped fluoride fiber lasers," IEEE J. Quantum Electron. **47**, 262–273 (2011).
7. H. Többen, "Room temperature cw fibre laser at 3.5 μm in Er^{3+}-doped ZBLAN glass," Elec. Lett. **28**, 1361–1362 (1992).
8. W. Hofle and H. Többen, "Analysis, measurement and optimization of threshold power of 3.5 μm ZBLAN-glass fiber lasers," Int. J. of Infrared and Millimeter Waves **14**, 1407–1424 (1993).
9. M. Pollnau and S. D. Jackson, "Advances in mid-infrared fiber lasers," in *Mid-Infrared Coherent Sources and Applications,* M. Ebrahim-Zadeh and I. T. Sorokina, ed. (Springer, 2008).
10. O. Henderson-Sapir, "Development of dual-wavelength pumped mid-infrared fibre laser," Ph.D. thesis, University of Adelaide (2015).
11. M. Pollnau and S. D. Jackson, "Energy recycling versus lifetime quenching in erbium-doped 3-μm fiber lasers," IEEE J. Quantum Electron. **38**, 162–169 (2002).
12. R. Caspary, "Applied rare-earth spectroscopy for fiber laser optimization," Ph.D. thesis, Technical University Braunschweig, Germany (2001).
13. L. Wetenkamp, G. F. West, and H. Többen, "Optical properties of rare earth-doped ZBLAN glasses," J. of Non-Crystalline Solids **140**, 35–40 (1992).
14. R. S. Quimby, W. J. Miniscalco, and B. A. Thompson, "Excited-state absorption at 980 nm in erbium-doped glass," Proc. SPIE, vol. 1581, pp. 72–79, (1992).
15. L. Jianfeng and S. D. Jackson, "Numerical modeling and optimization of diode pumped heavily-erbium-doped fluoride fiber lasers," IEEE J. Quantum Electron. **48**, 454–464 (2012).
16. U. Skrzypczak, M. Miclea, A. Stalmashonak, B. Ahrens, B. Henke, G. Seifert, J. A. Johnson, and S. Schweizer, "Time-resolved investigations of erbium ions in ZBLAN-based glasses and glass ceramics," Physica Status Solidi **8**, 2649–2652 (2011).

17. J. Li, L. Gomes, and S. D. Jackson, "Numerical modeling of holmium-doped fluoride fiber lasers," IEEE J. Quantum Electron. **48**, 596–607 (2012).
18. L. Jianfeng, L. Hongyu, L. Yong, Z. Lin, and S. D. Jackson, "Modeling and optimization of cascaded erbium and holmium doped fluoride fiber lasers," IEEE Sel. Top. in Quantum Electron. **20**, 15–28 (2014).

1. Introduction

Recently, significant progress has been made in extending the operation of fiber lasers into the mid-infrared, with lasers achieving over 30 W at 3 μm [1]. In a previous publication we demonstrated that dual wavelength pumping (DWP) could significantly increase the efficiency of erbium doped ZBLAN glass fiber lasers that operate on the 3.5 μm transition. We reported a continuous-wave (CW) output power in excess of 250 mW which was the first room temperature rare-earth doped fiber laser to produce more than 10 mW well beyond 3 μm [2]. Recently two groups have reported over 1 W of power at 3.5 μm using this approach [3, 4]. In this paper we report a new energy-transfer (ET) process that must be considered for the successful optimization of lasers that operate on the 3.5 μm transition in erbium using low phonon energy hosts.

The energy level structure of erbium is complex as there are many non-radiative energy-transfer processes. This complexity is particularly apparent when using glasses with low-phonon energies and radiative transitions that are located high above the ground state. These glasses reduce the rate of non-radiative decay allowing significant populations to be established in higher energy states thereby increasing the likelihood of energy-transfer processes.

Three energy exchange processes between erbium ions have been extensively investigated because they affect the performance of the commonly used erbium ion lasing transitions [5, 6]. The exchange processes are: ${}^4I_{13/2} + {}^4I_{13/2} \rightarrow {}^4I_{15/2} + {}^4I_{9/2}$ denoted here by W_{11}, ${}^4I_{11/2} + {}^4I_{11/2} \rightarrow {}^4I_{15/2} + {}^4F_{7/2}$ denoted by W_{22} and ${}^2H_{11/2} + {}^4I_{15/2} \rightarrow {}^4I_{9/2} + {}^4I_{13/2}$ commonly denoted in the literature by W_{50}. Figure 1 shows all considered spectroscopic processes. The strength of these interactions depend on the concentration of the dopant and must be accounted for when optimizing a fiber laser, since some are detrimental to lasing whilst others are beneficial [5].

Többen and Hofle reported 3.5 μm lasing on the ${}^4F_{9/2} \rightarrow {}^4I_{9/2}$ transition using ground state pumping by a 655 nm DCM dye laser [7, 8]. A maximum average output power of 8 mW with a slope efficiency of less than 3% at room temperature was reported. In our 3.5 μm DWP laser a pump operating at 985 nm (P_1) establishes a significant population of erbium ions in the metastable ${}^4I_{11/2}$ level. A second pump source P_2 excites these ions from the ${}^4I_{11/2}$ level to the upper lasing level, ${}^4F_{9/2}$. The ions emit laser radiation at 3.5 μm and relax from the lower lasing level ${}^4I_{9/2}$ to the ${}^4I_{11/2}$ level via rapid multi-phonon decay (MP). From here they are re-excited by P_2, with the ions cycling between the ${}^4I_{11/2}$ and ${}^4F_{9/2}$ levels many times, using the "virtual ground" state created in the ${}^4I_{11/2}$ level.

Developing this 3.5 μm fiber laser was more difficult than originally expected. The four-level nature of the transition should have allowed lasing with relatively modest levels of absorbed second pump P_2 at 1973 nm. The first unsuccessful attempts of lasing were undertaken using a heavily doped fiber with 4 $mol.\%$ of Er^{3+} ions that was available commercially. A study of absorbed power versus incident power at 1973 nm using a 6 cm long Er^{3+}:ZBLAN fiber suggested that we should have achieved a population inversion. An additional estimate of threshold based on Többen's results [7] suggested that threshold should have been achieved with an absorbed 1973 nm power of between 75 mW and 100 mW which was much less than the 200 mW power level that we used. Here we describe an investigation into a new energy exchange process that depletes ions from the ${}^4F_{9/2}$ level and reduces the inversion achieved.

This paper is organized as follows: We first present results that demonstrate that the lifetime of the $F_{9/2}$ is dependent on the dual-wavelength pumping conditions. These results demon-

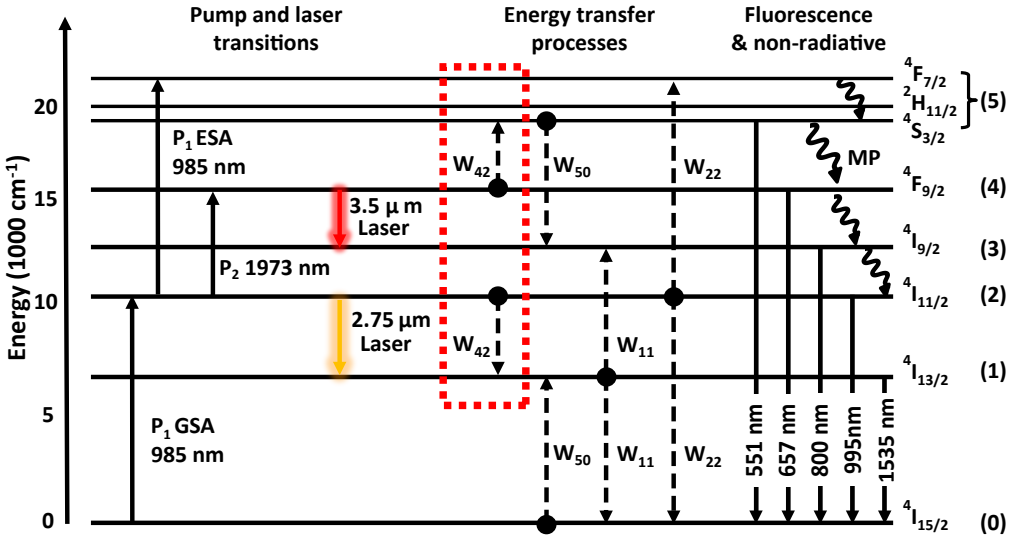

Fig. 1. Energy levels, wavelengths and spectroscopic processes in Er^{+3}:ZBLAN. $P_{1,2}$ - pump absorption with GSA/ESA are the ground and excited-state absorption. Energy-transfer processes are indicated by W_{ij} with the indices indicating the initial levels involved in the process, which are marked with black dots; MP - multi-phonon relaxation. The subject of this paper, the W_{42} energy-transfer process is highlighted. Fluorescence wavelengths shown are the ones used in our measurements, although each fluorescence band is significantly broader. The numbers in brackets to the right represent the number of the rate equation, presented in section 3, which is associated with this energy level. Note that $^4F_{7/2}$, $^4S_{3/2}$ and $^2H_{11/2}$ are thermally coupled and share the same rate equation.

strate that the lifetime is affected by the population of the virtual ground state ($I_{11/2}$). We then show that this is due to a previously undocumented energy-transfer process $^4F_{9/2} + ^4I_{11/2} \rightarrow {}^4S_{3/2} + {}^4I_{13/2}$. Energy arguments suggest that this process is exothermic and very likely to occur since the energy difference between the line centers of the initial and final states is less than the maximum phonon energy of ZBLAN glass ($550cm^{-1}$) [9]. We then measure the magnitude of this effect using two different erbium doping concentrations, and include the results in a new, more complete model of the laser.

2. Identification of new cross relaxation process

We start this section by describing the experimental techniques used to observe the change in relative population densities of the first five excited state of erbium and determine the factors affecting the lifetime of the states. This is achieved by analyzing the fluorescent light that results from the spontaneous radiative decay from these excited states directly to the ground state. The total emission in these bands is proportional to the population of these states. Fluorescence signals were obtained from the following bands: 551 *nm*, 657 *nm*, 800 *nm*, 995 *nm* and 1535 *nm* (see Fig. 1). A schematic of the experimental setup used for measuring the fluorescence is shown in Fig. 2. The DWP source used two pump lasers which were combined using a dichroic mirror, prior to being injected into the Er^{3+}:ZBLAN fiber using a launching aspheric lens [10]. One pump source (P_1) was a nominally 974 *nm* fiber coupled laser diode (Thorlabs PL980P330J) that had a fiber-Bragg-grating (FBG) with a wavelength of 985.23 *nm* (O/Eland 98-008-5-5503) spliced to it in place of its original FBG. The output power of P_1 was

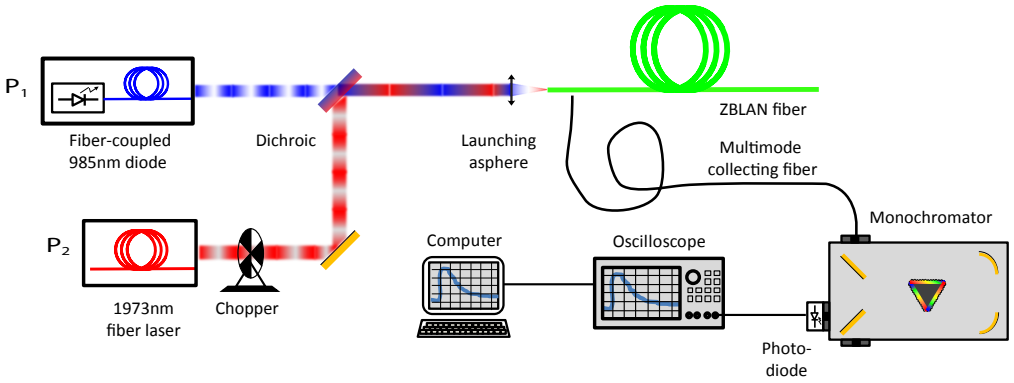

Fig. 2. Experimental setup for spectroscopy measurements.

300 mW, 65% of which was incident on the ZBLAN fiber using the DWP setup. The other pump laser (P_2) was a home-made 1973 nm fiber laser that was stabilized by a high-reflectivity FBG. Its output was an un-polarised, single transverse mode with a wavelength of 1973 nm when pumped with a 35 W, 790 nm fiber-coupled diode. The Er^{3+}:ZBLAN fiber was mounted in a groove in a fiber holder block.

The fluorescence emitted from the side of the ZBLAN fiber was collected by a large core (1 mm diameter), high numerical aperture (NA = 0.48), multi-mode fiber (Thorlabs BFH48-1000). The input end of the collecting fiber was located within 0.5 mm of the ZBLAN fiber and could be moved along the length of the ZBLAN fiber to collect fluorescence from various locations along the ZBLAN fiber, thus also enabling observation of the change in the fluorescence as a function of distance from the pump input side. The output from the collecting fiber was analyzed by a monochromator, resolving the different light bands corresponding to each state. In this configuration the resolution of the monochromator was 1nm, limited by the multi-mode fiber input but sufficient for this purpose.

The lifetime of the ${}^4F_{9/2}$ level was studied under a variety of P_1 and P_2 power levels. This was achieved by recording the 657 nm fluorescence as a function of time when the P_2 pump intensity was modulated. This enabled us to determine the total decay rate, or inversely, the combined lifetime of the ${}^4F_{9/2}$ level and show that a significant lifetime quenching process was taking place as a function of P_1 power.

The modulation of the intensity of the 1973 nm pump source was achieved by chopping it with a mechanical chopper wheel. The beam was chopped at 1 kHz, with an on time of 300 μs and an off time of 700 μs. This pump on-duration is two to three times the lifetime of the ${}^4F_{9/2}$ level (depending on pump condition), thus allowing for sufficient population build-up. The transition time of the chopper blade edge across the beam was measured to be 35 μs.

Datasets at each P_1 and P_2 power level combination were collected with an automated acquisition process, where 128 fluorescence decay waveforms at 657 nm were collected and averaged for each power level. These waveforms were read into a computer using our Matlab® application, which analyzed the waveforms and fitted an exponential decay with lifetime τ_{int} to each decay curve. The first 35 μs of the decay was not used in the fit due to transition time of the mechanical shutter edge across the beam. A separate set of measurements was conducted for two different fibers with dopant densities of 1.7 $mol.\%$ and 4 $mol.\%$.

An example of a typical measured decay of the $F_{9/2}$ state is shown in Fig. 3. The decay curve closely followed a single exponential decay, which means that the dominant process for removing ions from the $F_{9/2}$ state could not be an energy exchange process in which both ions

originated from the $F_{9/2}$ state, as discussed by Golding et al. [5]. Exponential decay is consistent with either a radiative decay, multi-phonon decay or an energy-transfer process which involves different energy levels.

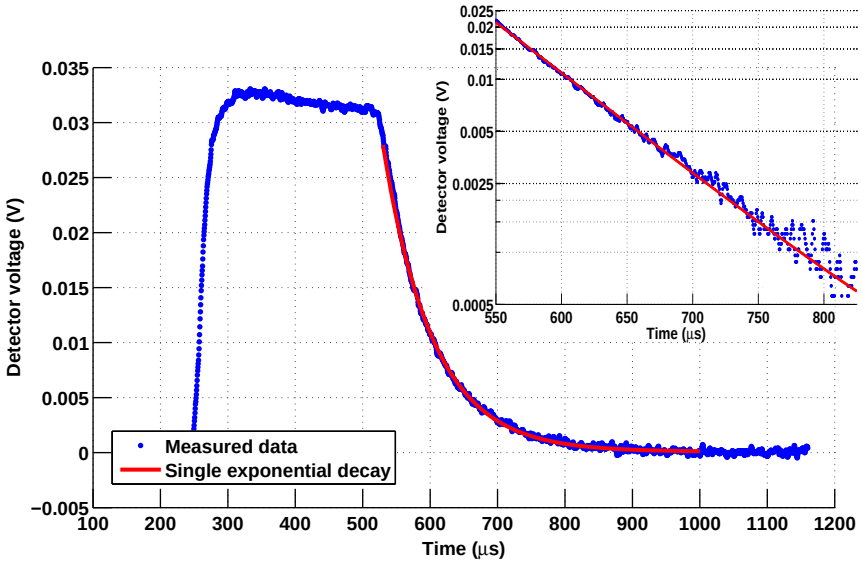

Fig. 3. An example of the decay of the population of the $^4F_{9/2}$ state as indicated by the intensity of the 657 *nm* fluorescence when the 1973 *nm* pump is blocked. The stronger fluorescence on the leading edge of the pulse is because of a temporary increase in the P_2 pump caused by different feedback conditions when blocking by the chopper was suddenly removed. The inset shows the decay part of the waveform on a semi-logarithmic plot. This example of the data was taken from a measurement with a FiberLabs ZDF fiber doped at 4 *mol.%*.

The measured lifetime of the $F_{9/2}$ state with differing incident P_1 and P_2 powers is illustrated in Fig. 4. This figure shows that the lifetime is strongly dependent on the incident P_1 light and virtually independent of the power of P_2. Similar behavior was obtained with fibers doped at 1.7 *mol.%* and 4 *mol.%*. This behavior was also observed when the fluorescence was collected at different locations along the fiber.

One possible explanation for the change in the lifetime of the $^4F_{9/2}$ state is an increase in multi-phonon non-radiative decay due to an increase in temperature. This can be ruled out, however because using DWP conditions, the dominant heat load in the fiber is due to the multi-phonon non-radiative decay $^4I_{9/2} \rightarrow {}^4I_{11/2}$ which is only significant when P_2 light is absorbed [10]. The observed independence of lifetime on the power of P_2 thus rules this out. Furthermore, the clear dependence on the power of P_1 alone strongly suggests that the lifetime quenching effect is dependent on the population of the $^4I_{11/2}$ state.

To investigate this claim further we examined the decay rate of the $^4F_{9/2}$ versus the population of the $^4I_{11/2}$ by using the fluorescence at 995 *nm* which is proportional to the population density of the $^4I_{11/2}$ energy level. This wavelength was chosen because it is not emitted by any other excited state and is sufficiently separated from the P_1 wavelength of 985 *nm* that the fluorescence could be separated from scattered pump light. The results of this investigation are presented in Fig. 5. This result shows the change in the decay rate is linearly proportional to the population of the $^4I_{11/2}$ state. This is consistent with an exchange process involving the $^4I_{11/2}$ and $^4F_{9/2}$ states. In the results that follow we present data that strongly indicated that the ions

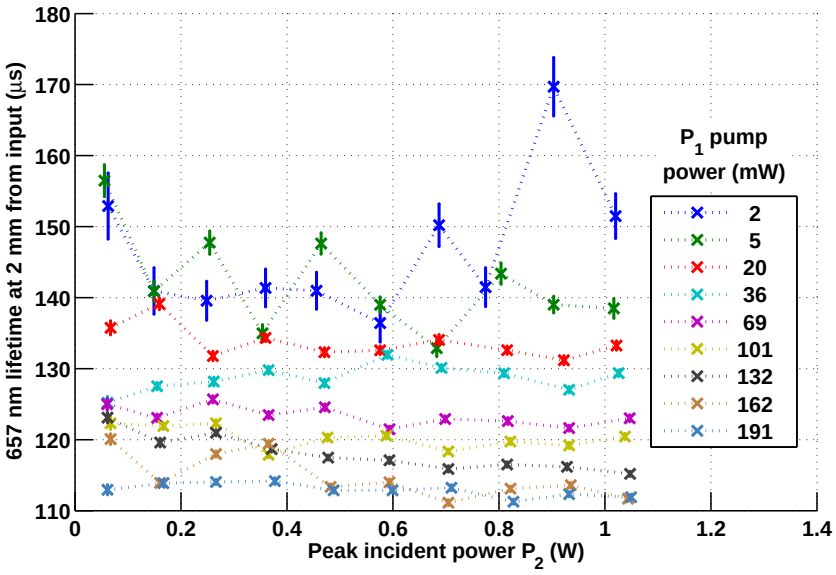

Fig. 4. Example of ${}^4F_{9/2}$ lifetime changes with pump power in IR-Photonics, 1.7 *mol.%* doped fiber. Each coloured curve represents a fixed P_1 pump power, while the P_2 pump power was increased. In this measurement the fluorescence was collected at 2 *mm* from the fiber input side.

are left in the ${}^4S_{3/2}/{}^2H_{11/2}$ and ${}^4I_{13/2}$ states. This is not a surprising result based on energy conservation arguments outlined earlier.

A second set of fluorescence measurements was conducted with increasing levels of incident P_1 and P_2, both CW. The purpose of this experiment was to find the relative change in population densities of the first five excited states obtained under varying combinations of P_1 and P_2 powers in order to verify the terminal states of the energy exchange process.

In these experiments we replaced the monochromator used previously with a Yokogawa ANDO AQ6315E optical spectrum analyzer (OSA) since large dynamic range was needed while rapid time response was not required. A Matlab® semi-automated procedure was used for retrieving and analyzing the wideband fluorescence data from the OSA. Since the OSA measures power and we were interested in the relative population of the levels, the results were normalized according to the different energies of photons at varying wavelength bands and thus accounted for the proportional excited ions population at the different energy levels. The collected fluorescence at each level is therefore proportional to the ion population density in the level.

A study of the population of the ${}^4S_{3/2}/{}^2H_{11/2}$ levels is presented in Fig. 6(a) which shows the increase in 551 *nm* fluorescence versus the product of the fluorescence from the ${}^4I_{11/2}$ and ${}^4F_{9/2}$ states for a variety of differing combinations of P_1 and P_2 pump power. The energy transfer rate for an ET process is proportional to the product of the population densities of the initial states. Hence, when an ET process is the dominant mechanism for filling a state, the population will be proportional to the product of the density of the initial states of the ET process. In our case the ${}^4S_{3/2}/{}^2H_{11/2}$ state is populated by this new ET mechanism, excited state absorption of P_1 photons by ions in the ${}^4I_{11/2}$ state and the energy exchange process W_{22}. The points closest to

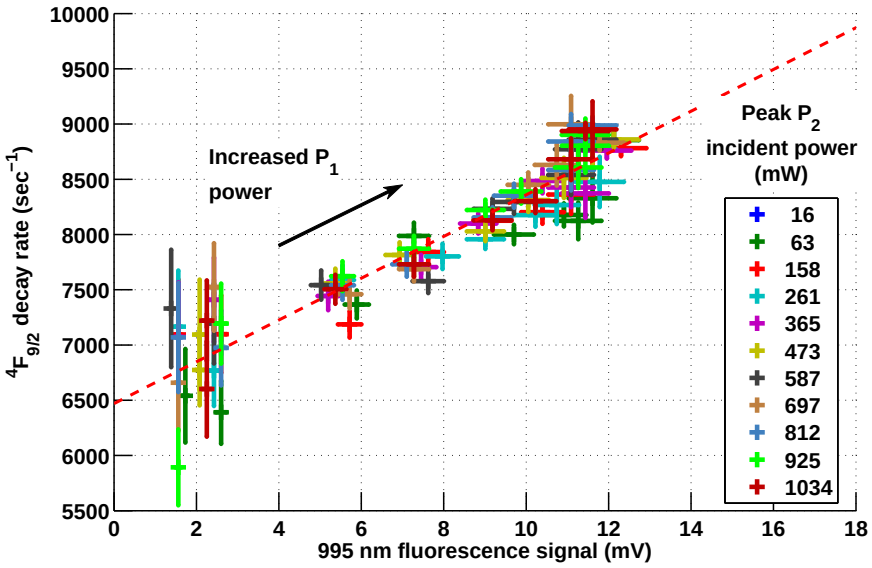

Fig. 5. Decay rate of the $^4F_{9/2}$ level as a function of the relative population density of the $^4I_{11/2}$ state as measured by the intensity of 995 *nm* fluorescence in a 1.7 *mol.%* doped fiber. Markers of the same color represent readings taken with a fixed P_2 while P_1 power was changed. The spread in the data at the low 995 *nm* fluorescence is because of reduced population at the $^4I_{11/2}$ state ions and hence poor absorption of P_2 light.

the left hand side of this plot are for when the power of P_2 is zero and hence the population of the $^4S_{3/2}/^2H_{11/2}$ state and the $^4F_{9/2}$ state are filled by excited state absorption and the ET process W_{22}. The next points across represent a P_2 power of 50 *mW* (about one twentieth of the maximum power used in the measurements) which show the data joining the new linear trend indicated by the lower dotted lines meaning for this power level the dominant excitation mechanism is the new ET process. Further increases in P_2 power depletes ions from the $^4I_{11/2}$ level which are efficiently replaced by ground state ions that absorb light from P_2. This means increasing P_2 effectively depletes ions from the ground state meaning that the rate of the ET process W_{50} decreases, thereby increasing the population of the $^4S_{3/2}/^2H_{11/2}$ state.

A study of the populating of the $^4I_{13/2}$ state is presented in Fig. 6(b). The points closest to the left are for the situation when P_2 was switched off. In this situation the population of the $^4I_{13/2}$ state is established by fluorescent decay from the state above. This rapidly changes with increasing the power of P_2 which decreases the population of the $^4I_{11/2}$ state but increases the population of the $^4F_{9/2}$ state.

It is worth noting that for all fixed P_1 power levels the fluorescence increases linearly as the power of P_2 increases. This is strong evidence for this ET process. Since if the dominant transfer process to the $^4I_{13/2}$ state was direct fluorescence and/or multi-phonon relaxation from the $^4I_{11/2}$ state then the population of the $^4I_{13/2}$ state should decrease with the reduction in the population of the $^4I_{11/2}$ state that would occur with increased P_2 pumping. In addition, if the previously known ET processes W_{11} and W_{22} were playing a significant part, they would have also caused a reduction in the $^4I_{13/2}$ fluorescence. W_{11} would have done that by directly

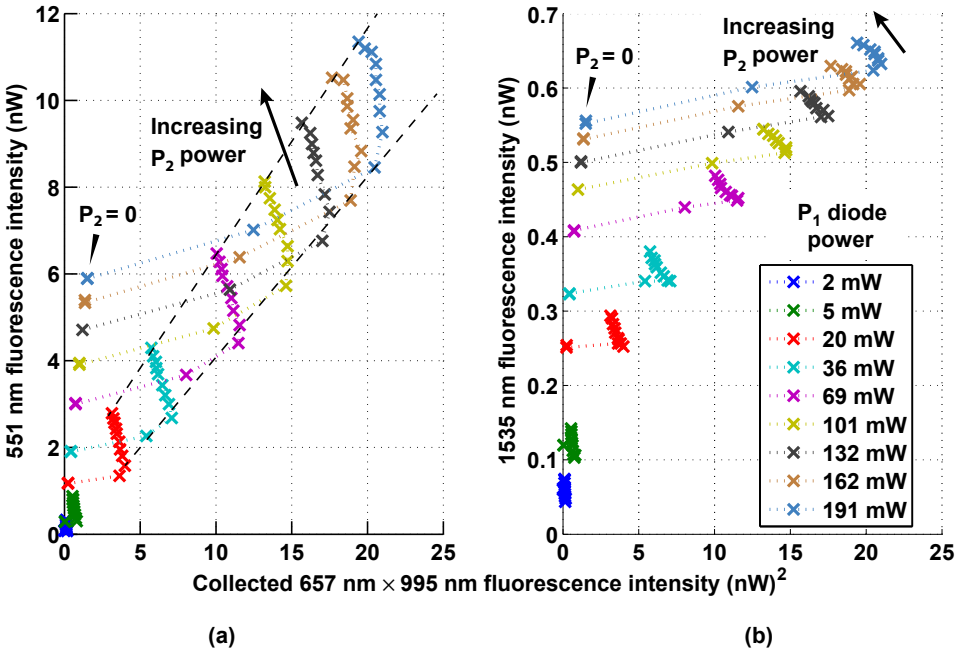

Fig. 6. Fluorescence at 551 *nm* and 1535 *nm* collected from the side of the 1.7 *mol.%* doped fiber as an indicator for energy level population. Fluorescence collected at 2 *mm* from the input side of the fiber.

depopulating the ${}^4I_{13/2}$ state, while W_{22} by reducing the population of ${}^4I_{11/2}$ which feeds ${}^4I_{13/2}$ via fluorescence.

3. Quantification of the new cross relaxation process

In this section, we lay out the theoretical framework required to measure the value of the ET parameter (W_{42}). We use a numerical model to convert our measured fluorescence curves into absolute population densities. This approach was chosen because a direct measurement of the absolute population densities and absorbed light in a single fiber element is difficult. Such a measurement requires an exact and wavelength dependent calibration of the fiber collection efficiency, the OSA and the pump launching efficiency.

The following rate equations describe the relevant population dynamics of Er^{3+}:ZBLAN. The dependence of the parameters on the location along the fiber was used in the simulation

but is omitted here for brevity.

$$dN_5/dt = R_{P_1\,ESA} + W_{22}N_2^2 - \tau_5^{-1}N_5 - W_{50}N_5N_0 + W_{42}N_2N_4, \tag{1a}$$

$$dN_4/dt = R_{P_2} + \beta_{54}\tau_5^{-1}N_5 - \tau_4^{-1}N_4 - W_{42}N_2N_4, \tag{1b}$$

$$dN_3/dt = \beta_{53}\tau_5^{-1}N_5 + \beta_{43}\tau_4^{-1}N_4 - \tau_3^{-1}N_3 + W_{50}N_5N_0 + W_{11}N_1^2, \tag{1c}$$

$$dN_2/dt = R_{P_1\,GSA} - R_{P_1\,ESA} - R_{P_2} + \Sigma_{i=3\ldots5}[\beta_{i2}\tau_i^{-1}N_i] - \tau_2^{-1}N_2 - 2W_{22}N_2^2 - W_{42}N_2N_4, \tag{1d}$$

$$dN_1/dt = \Sigma_{i=2\ldots5}[\beta_{i1}\tau_i^{-1}N_i] - \tau_1^{-1}N_1 + W_{50}N_5N_0 - 2W_{11}N_1^2 + W_{42}N_2N_4, \tag{1e}$$

$$dN_0/dt = \Sigma_{i=1\ldots5}[\beta_{i0}\tau_i^{-1}N_i] - R_{P_1\,GSA} - W_{50}N_5N_0 + W_{11}N_1^2 + W_{22}N_2^2, \tag{1f}$$

$$N_{Er} = \Sigma_{i=0\ldots5}N_i. \tag{1g}$$

In these equations, N_i is the ion density of the i^{th} energy levels, $R_{P_1\,GSA}$ and R_{P_2} are the pump rates of P_1 at 985 *nm* and P_2 at 1973 *nm*, respectively. $R_{P_1\,ESA}$ represent the excited-state absorption rate of pump P_1 on the ${}^4I_{11/2} \rightarrow {}^4F_{7/2}$ transitions. All the pump rates (R) are dependent on pump power and their exact forms are given below. τ_i is the intrinsic lifetime of the i^{th} energy levels, including radiative and multi-phonon relaxation. W_{ij} describes the energy-transfer process of two ions out of levels i and j. β_{ij} is the branching ratio, or the probability an ion decays from level i into level j. N_{Er} is the Er^{3+} ion doping density in the fiber. We assume that all ions that are excited to the ${}^4F_{7/2}$ level are rapidly distributed within the thermally connected ${}^4F_{7/2} + {}^2H_{11/2}/{}^4S_{3/2}$ manifolds via fast multi-phonon decays, all of which are treated as a single level. Only one of the Eqs. (1f) or (1g) is needed to solve the equation set but for completeness they are both given here. The spectroscopic parameters used in our simulation are given in Table 1.

Many of the parameters used in Eqs. (1a)-(1f) can be found in the literature, for example [11, 12, 13]. These include the energy level lifetimes τ_i, branching ratios β_{ij} and numerous rates for ET processes W_{ij}.

The ground-state absorption (GSA), and excited-state absorption (ESA) rates for P_1 and P_2 pumps along each fiber segment can be characterized by

$$R_{P_1 GSA} = (\sigma_{0,2}N_0 - \sigma_{2,0}N_2)\frac{\lambda_{p_1}}{hc\pi r_{core}^2}P_{in1}, \tag{2a}$$

$$R_{P_1 ESA} = (\sigma_{2,5}N_2 - \sigma_{5,2}N_5)\frac{\lambda_{p_1}}{hc\pi r_{core}^2}P_{in1}, \tag{2b}$$

$$R_{P_2} = (\sigma_{2,4}N_2 - \sigma_{4,2}N_4)\frac{\lambda_{p_2}}{hc\pi r_{core}^2}P_{in_2}, \tag{2c}$$

where $\sigma_{i,j}$ with $i < j$ represent the pump absorption cross-section from the N_i level to the N_j level, while $\sigma_{i,j}$ with $i > j$ are the emission cross-sections of the inverse processes. $P_{in_{1,2}}$ are both pumps power incident on the appropriate fiber segment, $\lambda_{p_{1,2}}$ are the pump wavelengths, h is Planck's constant, c is the speed of light in vacuum, and r_{core} is the fiber core radius.

Values of the ground state absorption $\sigma_{0,2}$ and excited state absorption $\sigma_{2,5}$ over the entire wavelength range of 970 *nm*-1000 *nm* are available from measurements by Quimby and Miniscalco [14]. The inverse processes were calculated from these values using the McCumber relations [12]. The values of $\sigma_{2,4}$ and $\sigma_{4,2}$ can be found in [10].

The previously established ET parameters, which were measured in bulk ZBLAN glass by Golding et al. [5], are on the order of $10^{-17}\ cm^3/s$ and are henceforth referred to as the "strongly interacting" (SI) parameters. These values were used extensively in the literature until recently

when a new, "weakly interacting" (WI) approach was introduced by Gorjan et al. [6] and later extended by Li and Jackson [15]. The WI approach asserts that ET processes are considerably weaker in ZBLAN fibers than in bulk glass, with values on the order of $5 \times 10^{-19}\ cm^3/s$. The WI-based ET parameter values were found numerically by Gorjan et al. when fitting experimental data to a set of rate-equations. Both approaches are currently in use and values of ET parameters for both are presented in Table 2.

Table 1. Parameters used throughout the simulations.

Parameter	Value	Source
$\tau_1,\ \tau_2,\ \tau_3\ [ms]$	9.0, 6.9, 0.01	[15]
$\beta_{21},\ \beta_{20}$	0.37, 0.63	[15]
$\beta_{32},\ \beta_{31},\ \beta_{30}$	0.99, 0, 0.01	[15]
$\beta_{43},\ \beta_{42},\ \beta_{41},\ \beta_{40}$	0.85, 0.006, 0.004, 0.14	[15]
$\beta_{54},\ \beta_{53},\ \beta_{52},\ \beta_{51},\ \beta_{50}$	0.34, 0.012, 0.015, 0.18, 0.44	[15]
$\lambda_{p1}\ [nm]$	985	[10]
$\lambda_{p2}\ [nm]$	1973	[10]
$\sigma_{0,2}\ [cm^2]$	0.93×10^{-21}	[14]
$\sigma_{2,5}\ [cm^2]$	0.17×10^{-21}	[14]
$\sigma_{2,0}\ [cm^2]$	1.1×10^{-21}	[14, 12]
$\sigma_{5,2}\ [cm^2]$	0.7×10^{-21}	[14, 12]

Parameter	1.7 $mol.\%$ Er^{3+} fiber	4 $mol.\%$ Er^{3+} fiber	Source
$\tau_4\ [\mu s]$	237	170	[16]
$\tau_5\ [\mu s]$	570	100	[16]
$W_{11}\ [cm^3/s]$, (WI)	0.4×10^{-18}	0.6×10^{-18}	Table 3
$W_{22}\ [cm^3/s]$, (WI)	0.1×10^{-18}	0.2×10^{-18}	Table 3
$W_{50}\ [cm^3/s]$, (WI)	0.17×10^{-18}	0.38×10^{-18}	Table 3
$W_{11}\ [cm^3/s]$, (SI)	1.4×10^{-17}	2.2×10^{-17}	Table 3
$W_{22}\ [cm^3/s]$, (SI)	0.3×10^{-17}	0.8×10^{-17}	Table 3
$W_{50}\ [cm^3/s]$, (SI)	0.8×10^{-17}	1.9×10^{-17}	Table 3
$N_{Er}\ [ions/cm^3]$	2.72×10^{20}	6.40×10^{20}	Supplier
$r_{core}\ [\mu m]$	5	7	Supplier

Table 2. Macroscopic known energy transfer parameters in Er^{3+}:ZBLAN for different doping concentrations. Parameters from two regimes are included: strongly interacting (SI) [5] and weakly interacting parameters (WI) [15]. Energy transfer parameters relevant to this work, which fall in between values found in literature, were interpolated (*) or extrapolated (‡) according to the curves provided in [5, 15].

	Parameter	Value						
	$Er^{3+}\ mol.\ \%$	0.25	1	1.25	1.7	4	5.00	8.75
	$Er^{3+}\ \times 10^{20}\ ions/cm^3$	0.4	1.6	2	2.7	6.4	8	14
SI	W_{50}	0.6	0.48*	0.6	0.8*	1.9*	2.4	3.3
	$W_{11}\quad \times 10^{-17}\ cm^3/s$		1.3‡	1.3	1.4*	2.2*	2.8	6.7
	W_{22}		0.16‡	0.2	0.3*	0.8*	1.0	1.9
WI	W_{50}		0.1‡	0.12‡	0.17‡	0.38	0.46*	0.6
	$W_{11}\quad \times 10^{-18}\ cm^3/s$		0.4‡	0.4‡	0.4‡	0.6	0.8*	1.8
	W_{22}		0.08‡	0.09‡	0.1‡	0.2	0.26*	0.43

Recent numerical analysis based on the WI approach has been successful in reproducing experimental results that could not be explained using an SI-based numerical analysis in ZBLAN fiber lasers [6, 15, 17, 18]. During our spectroscopic investigations, both sets of parameters were used where applicable and the results compared.

Pumping with P_1 light establishes a population in the ${}^4I_{11/2}$ state but it also establishes populations in the other states through excited state absorption, decay and ET processes. Excited state absorption from the ${}^4I_{11/2}$ state is reduced when pumping with 985 *nm*, compared with the typical pumping wavelength of 974 *nm*, but is not eliminated all together [14]. Hence, with steady state 985 *nm* pumping we establish mean populations in the states which are denoted $\bar{N}_i$. The associated change of the state populations when Er:ZBLAN is pumped with a chopped second pump can be treated as a perturbation ΔN_i about the population means $(\bar{N}_i)$. The equation that describes the decay of the perturbation of the ${}^4F_{9/2}$ state when the P_2 beam is chopped is given by:

$$d\Delta N_4/dt = -\Delta N_4(\tau_4^{-1} + W_{42})\bar{N}_2 + \beta_{54}\tau_5^{-1}\Delta N_5. \tag{3}$$

The last term in Eq. (3) would prevents us from finding a simple exponential solution and in what follows we argue that it is small and can be neglected. When using DWP the majority of the population of ΔN_4 comes from direct excitation by the second pump which is different to the singly pumped case where the very small N_4 population tracks the N_5 population because it is fed by multi-phonon decay from N_5. The branching ratio of the ${}^4S_{3/2}/{}^2H_{11/2} \rightarrow {}^4F_{9/2}$ is small ($\beta_{54} = 0.25$) [12] which further reduces the effect of this term. The intrinsic lifetime of the ${}^4S_{3/2}/{}^2H_{11/2}$ levels, τ_5, depends on the Er^{3+} concentration and varies between 560 μs at very low doping concentrations to ~ 15 μs at very high ones (9 *mol.%*) [16]. This decrease in lifetime is due to increases in the rate of ET processes such as the W_{50}. These processes empty the ${}^4S_{3/2}/{}^2H_{11/2}$ state but do not terminate in the ${}^4F_{9/2}$ state thereby reducing the effect of the last term in Eq. (3) further.

Our measurements show that N_2 population does reduce with increased P_2 pumping. At the lower levels of the P_2 power, the change in N_2 population is on the order of 10%, which can be deemed as a small perturbation to the decay waveform, maintaining an exponential decay. It is interesting to note that at the highest P_2 power used of over 1 W, N_2 exhibited close to 40% reduction in population (as measured by 995 *nm* fluorescence), yet the measured lifetime still showed a very consistent exponential decay waveform, as seen in Fig. 3. Under these conditions of effectively a constant N_2 population the solution to Eq. (3) follows a simple exponential decay with a time constant of the form,

$$\Delta N_4(t) = \Delta N_4(0)e^{-(\frac{1}{\tau_4} + W_{42}N_2)t}. \tag{4}$$

Hence, to determine the new energy exchange coefficient we need to determine the decay constant of the perturbation to the ${}^4F_{9/2}$ level for a variety of accurately determined N_2 populations. To find the absolute population densities of the different energy levels as a function of P_1, we started with the fluorescence measurements as a function of both P_1 and P_2 described at the end of section 2. These fluorescence readings were only proportional to the ion population density and a scaling factor to the absolute population density was required.

The scaling factor was obtained by using the observed fluorescence with P_2 turned off. The OSA readings of each wavelength band were normalized to the population densities predicted by a simple rate-equation simulation. The simulation calculated the expected population density along the fiber by solving the system of Eqs. (1a)-(1f), (2a), (2b). Normalization factors between the fluorescence readings and the absolute population density were determined based on the fluorescence obtained with the second lowest P_1 power measured. This power level was advantageous because fluorescence was sufficiently high to obtain low measurement uncertainty.

In addition, the simulated results were not affected significantly by excited state absorption and energy exchange processes because of the relatively low population densities created at this power level.

The normalization created a one-to-one relation between observed fluorescence when only P_1 was used and the ion population density at a certain energy level. An example of the agreement between the observed fluorescence and the shape of the curves can be seen in Fig. 7. Significantly better agreement was achieved for the population of the $^4F_{9/2}$ level once the appropriate ET factor (found later in this section) was included in the simulation (see dashed lines in Fig. 7).

We chose to use this population normalization method for multiple reasons. First, a numerical analysis can predict the variations along the fiber, while simple calculations which assume average values cannot account for them. Secondly, directly fitting a power level measured with the OSA to a known population overcomes the compound effects of the detector response, fiber attenuation and OSA grating and detector calibration (assuming their linearity, which was verified) all with their respective (and sometimes unknown and difficult to measure) wavelength dependencies.

Figure 7 is an example of scaling curves as explained above. The scaling used both simulated and measured results using the first pump only. In addition, different scaling curves were produced by the SI and WI regimes, which resulted in different simulated population densities at the power levels measured in our experiments (see Fig. 7 inset). The measured intensities (squares in Fig. 7) at the various energy levels were superimposed on the simulated values (curves) and a scaling factor between the two was established. The appropriate factors were maintained for each level with the same measured and simulated conditions when conducting measurements using DWP conditions.

In our rate equation simulations we used both the commonly used SI and WI parameter values because both approaches are still in use. We obtained different fitted ET values based on population density normalization using both approaches. The values of the literature ET parameters used in our normalizations can be found in Table 2.

Once the absolute population densities were known we could obtain the values of the W_{42} ET constant using the previously found lifetime of the $^4F_{9/2}$ state and Eq. (4). A linear fit was used to obtain the W_{42} constant, which is the slope of the fit. An example for this fit can be seen in Fig. 8.

We obtained a linear fit between the normalized population with P_1 and $^4F_{9/2}$ decay rates for all combinations of experimental and measured data analyzed. The only free parameters in our fit were the ET constant W_{42} and the intrinsic lifetime of the $^4F_{9/2}$ level. The values obtained for the W_{42} ET constant based on the WI and SI assumptions are shown in Table 3. We estimate an uncertainty of approximately 20% in the ET values due to the sensitivity of the simulated population density of $^4I_{11/2}$ to various parameters, most of which are not known precisely or are not quoted with uncertainty values in the literature. A sensitivity analysis showed that the parameters most susceptible to affecting the simulated population are the ZBLAN fiber core diameter (manufacturer tolerance of 10% along the fiber), launch efficiency of P_1 pump (up to 10% tolerance assumed) and the W_{22} ET process (50% uncertainty assumed) all resulting in uncertainties of 15%, 10% and 10% respectively.

4. Discussion

Table 3 displays results for the ET constant results obtained with both 1.7 $mol.\%$ and 4 $mol.\%$ fibers. Although other ET parameters are considerably different between the SI and WI regimes, both approaches provided our newly reported ET process constants average with the same order of magnitude: 2.5 and 3.0 $\times 10^{-17}$ cm^3/s for SI and about 1.5×10^{-17} cm^3/s for WI. The

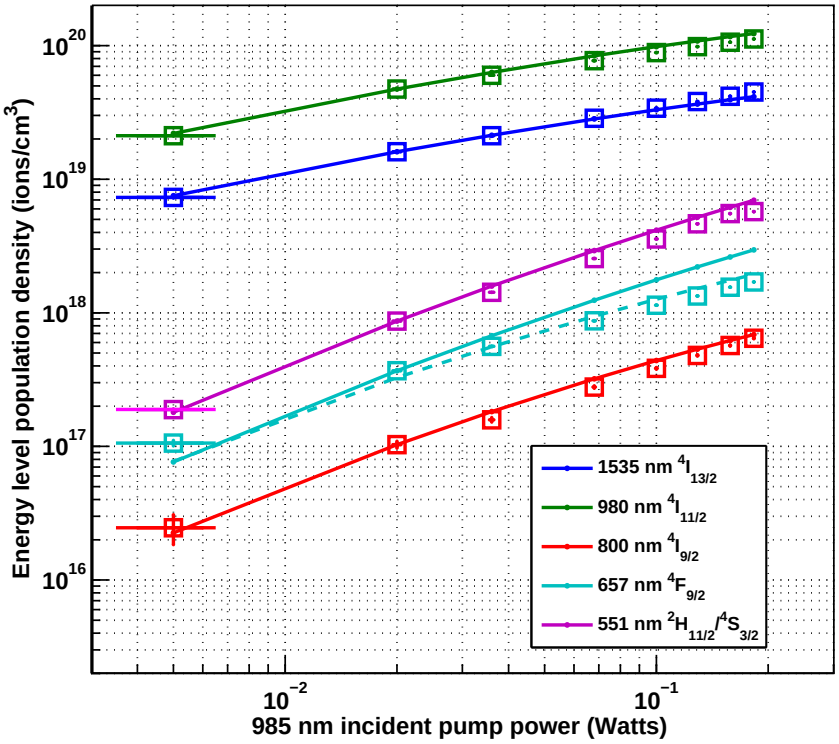

Fig. 7. The populations density of the bottom five excited states of Er:ZBLAN versus incident P_l power using the WI parameters assumptions in a 4 *mol.%* doped fiber. The continuous curves represent the simulated results assuming $W_{42} = 0$. The dashed line for the $^4F_{9/2}$ level represents the simulated values assuming W_{42} as measured. The squares are the measured fluorescence signals and their uncertainties scaled to the absolute population using simulated population at the second data point using WI regime.

Table 3. Energy-transfer coefficient $^4F_{9/2} + ^4I_{11/2} \rightarrow ^4S_{3/2} + ^4I_{13/2}$. Comparison of all values obtained using IR-Photonics fiber containing 1.7 *mol.%* of Er^{3+} ions and FiberLabs ZDF fiber containing 4 *mol.%* of Er^{3+} ions. Results for both the SI and WI approaches are shown. Uncertainty of these values is estimated at about 20%.

Er^{3+} concentration	ET strength assuming WI $(\times 10^{-17} cm^3)/s$	ET strength assuming SI $(\times 10^{-17} cm^3)/s$
1.7 *mol.%*	1.7 ± 0.15	2.5 ± 0.4
4 *mol.%*	1.55 ± 0.05	3.1 ± 0.1

relatively large ET factor of the $^4F_{9/2} + ^4I_{11/2} \rightarrow ^4S_{3/2} + ^4I_{13/2}$ process is not surprising because of the high absorption and emission cross-sections of both levels involved. With the current results, it did not seem that there was a clear dependency on the Er^{3+} concentration, although this could not be ruled out due to the uncertainties in the calculated values.

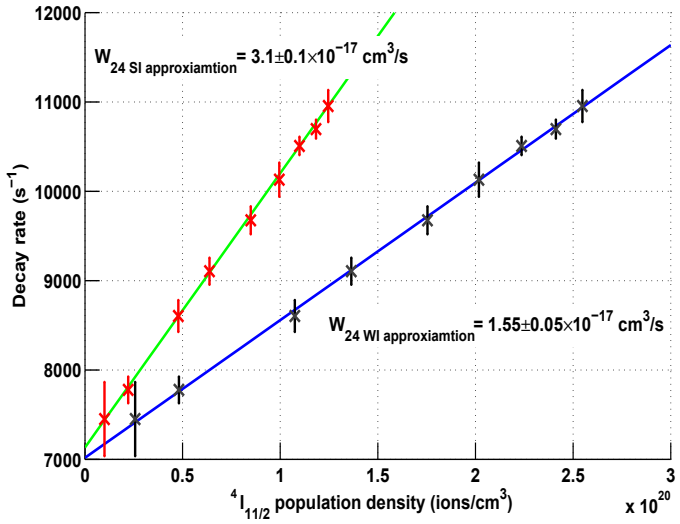

Fig. 8. Fit of decay rate to energy-transfer constant. This example is using values for the 4 $mol.\%$ doped fiber.

This new energy exchange process is likely to be responsible for the poor efficiency of the single wavelength pumped 3.5 μm laser reported by Többen [7]. In Többen's laser ions were bottlenecking in the $^4I_{11/2}$ and $^4I_{13/2}$ levels because of the multi-phonon cascades from the $^4F_{9/2}$ level. The new energy exchange process would have removed ions from the $^4F_{9/2}$ and $^4I_{11/2}$ levels leading to higher threshold and reduced efficiencies.

This new ET process is particularly problematic for dual-wavelength pumped lasers because it removes ions from both the upper laser and the virtual ground states. Removing ions from the virtual ground state means significantly higher powers of P_1 are required for the efficient absorption of P_2. The impact of this ET process was reduced in recent work [3, 4] that used lower doping densities and double clad fibers which resulted in lower population densities at the $^4F_{9/2}$ and $^4I_{11/2}$ states. The combination of this and increased P_1 power removed the laser power saturation that was observed in our earlier work [2].

A complete numerical model is needed to quantify the impact of this ET process on the performance of Er^{3+} lasers that use $^4F_{9/2} \rightarrow {}^4I_{9/2}$ transition. Currently we are in the process of developing such a model that incorporates all known processes in Er:ZBLAN including laser action. This model will be used to compare the experimental results described in [2] and will be reported in a future publication.

5. Conclusion

In this paper we investigated a previously undocumented ET mechanism in Er:ZBLAN, namely the $^4F_{9/2} + {}^4I_{11/2} \rightarrow {}^4S_{3/2} + {}^4I_{13/2}$ process. We characterized this process and measured its strength for the case of two erbium doping concentrations in Er:ZBLAN.

This ET process can strongly affect the performance of the $^4F_{9/2}$ to $^4I_{9/2}$ lasing transition in erbium doped glass lasers because it efficiently removes ions from the top lasing state. It is doubly harmful for dual wavelength pumped lasers because it also ejects ions from the virtual ground state. This process must be taken into account when the performance of these lasers is modeled. These finding mean that efficient mid-infrared lasers that lase on the $^4F_{9/2}$ to $^4I_{9/2}$ transition must be lightly doped to minimize the effect of this ET process.

Acknowledgments

The authors acknowledge the financial support of the South Australian Government through the PSRF and PRIF schemes.